

Learning Distributions on Manifolds with Free-form Flows

Peter Sorrenson*, Felix Draxler*, Armand Rousselot*, Sander Hummerich, Ullrich Köthe
Computer Vision and Learning Lab, Heidelberg University

*equal contribution, `firstname.lastname@iwr.uni-heidelberg.de`

Abstract

Many real world data, particularly in the natural sciences and computer vision, lie on known Riemannian manifolds such as spheres, tori or the group of rotation matrices. The predominant approaches to learning a distribution on such a manifold require solving a differential equation in order to sample from the model and evaluate densities. The resulting sampling times are slowed down by a high number of function evaluations. In this work, we propose an alternative approach which only requires a single function evaluation followed by a projection to the manifold. Training is achieved by an adaptation of the recently proposed free-form flow framework to Riemannian manifolds. The central idea is to estimate the gradient of the negative log-likelihood via a trace evaluated in the tangent space. We evaluate our method on various manifolds, and find significantly faster inference at competitive performance compared to previous work. We make our code public at <https://github.com/vislearn/FFF>.

1. Introduction

In recent years, generative models have achieved remarkable success in various domains like image synthesis [44], natural language processing [6], science [39] and more. However, the approaches are not naively applicable when dealing with data inherently structured in non-Euclidean spaces, particularly prevalent in fields such as the natural sciences and computer vision. Examples of such data are earth science data supported on a sphere, angles between functional groups in proteins, which are naturally represented on a torus, as well as the orientation of real world objects given as a rotation matrix in $SO(3)$. Naively, data on such an n -dimensional manifold \mathcal{M} can be represented using internal coordinates such as angles. However, this may not respect the topology, causing discontinuities or artifacts.

Luckily, many generative models can be generalized to

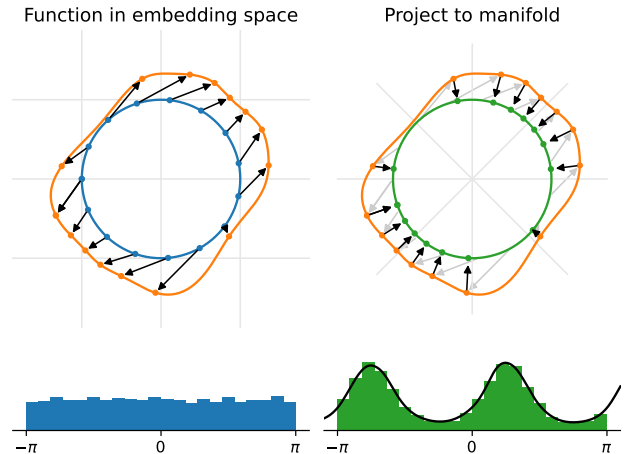


Figure 1. Manifold free-form flows (M-FFF) learn a distribution directly on the manifold via a generator network in the embedding space $\tilde{g}_\phi : \mathbb{R}^m \rightarrow \mathbb{R}^m$ (top left) whose outputs are projected to the manifold (top right). In this example, a uniform distribution (bottom left) is mapped to a bimodal distribution on the circle (bottom right), which we show as a histogram over model samples and the learned density as a function of the angle. The embedding conserves the topology so that the resulting distribution is periodic and continuous everywhere.

arbitrary manifolds. Most existing methods involve solving differential equations, either stochastic (SDEs) or ordinary (ODEs), for sampling and density estimation such as [8, 10, 20, 30, 45]. While theoretically sound, these approaches are computationally intensive due to the need for numerous function evaluations during integration, slowing down sampling.

In this paper, we introduce a novel approach for modeling distributions on arbitrary Riemannian manifolds that circumvents the computational burden of previous methods. We achieve this by using a single feed-forward neural network on an embedding space as a generator whose outputs are projected to the manifold Fig. 1. We learn this network as a normalizing flow, made possible through adapting the free-form flow framework [11], recently proposed for Euclidean spaces, to Riemannian manifolds. The

core change is estimating the gradient of the negative log-likelihood within the tangent space of the manifold.

In particular, we make the following contributions:

- We adapt free-form flows to Riemannian manifolds, yielding manifold free-form flows (M-FFF) in Sec. 4. The model is trained end-to-end and involves only a single function evaluation in training and sampling.
- We demonstrate the model’s quality and speed on several manifold benchmarks, such as rotation matrices, earth data, and molecular torsion angles in Sec. 5. We find competitive quality to recent work at typically two orders of magnitude faster sampling.

Together, manifold free-form flows are a novel approach for learning distributions on manifolds. They are applicable to any Riemannian manifold with a known embedding and projection.

2. Related work

Existing work on learning distributions on manifolds can be broadly categorized as follows: (i) leveraging Euclidean generative models; (ii) building specialized architectures that respect one particular kind of geometry; and (iii) learning a continuous time process on the manifold. We compare our method to these approaches in Tab. 1 and give additional detail below.

Euclidean generative models. One approach maps the n -dimensional manifold to \mathbb{R}^n and learns the resulting distribution [17]. Another approach generalizes the reparameterization trick to Lie groups by sampling on the Lie algebra which can be parameterized in Euclidean space [16]. These approaches come with the downside that a Euclidean representation may not respect the geometry of the manifold sufficiently, e.g. mapping the earth to a plane causes discontinuities at the boundaries. This can be overcome by learning distributions on overlapping charts that together span the full manifold [23]. An orthogonal solution is to embed the data and add noise to it in the off-manifold directions, so that the distribution can be learnt directly in an embedding space \mathbb{R}^m [5]; this only gives access to an ELBO instead of the exact density. Our method also works in the embedding space so that it respects the geometry of the manifold, but directly optimizes the likelihood on the manifold.

Specialized architectures take advantage of the specific geometry of a certain kind of manifold to come up with special coupling blocks for building normalizing flows such as $SO(3)$ [27], $SU(n)$, $U(n)$ [3, 24]; hyperbolic space [2]; and tori and spheres [43]. Manifold free-form flows are not restricted to one particular manifold, but can be easily applied to any manifold for which an embedding and a projection to the manifold is known. As such, our model is an alternative to all of the above specialized architectures.

Continuous time models build a generative model based on parameterizing a ODE or SDE on any Riemannian manifold, meaning that they specify the (stochastic) differential equation in the tangent space [1, 8, 10, 14, 15, 20, 28, 30, 45]. These methods come with the disadvantage that sampling and density evaluation integrates the ODE or SDE, requiring many function evaluations. Our manifold free-form flows do not require repeatedly evaluating the model, a single function call followed by a projection is sufficient.

	Respect topology	Single step sampling	Arbitrary manifolds
Euclidean	✗	✓	✓
Specialized	✓	✓	✗
Continuous time	✓	✗	✓
M-FFF (ours)	✓	✓	✓

Table 1. Comparison of generative models on manifolds. We give a “✓” if any method in a category meets this requirement.

At its core, our method adapts the recently introduced free-form flow (FFF) framework [11] based on an estimator for the gradient of the change of variables formula [46]. We give more details in Sec. 3.1.

At its core, our method adapts the recently introduced free-form flow (FFF) framework [11] based on an estimator for the gradient of the change of variables formula [46]. We give more details in Sec. 3.1.

3. Background

In this section, we give some background for our method: We present an introduction to free-form flows, followed by Riemannian manifolds and distributions thereon.

3.1. Free-form flows

Free-form flows are a generative model that modify normalizing flows to work with arbitrary feed-forward neural network architectures [11]. Traditionally, normalizing flows are based on invertible neural networks (INNs) that learn an invertible transformation $z = f_\theta(x)$ from data $x \in \mathbb{R}^n$ to latent codes $z \in \mathbb{R}^n$. This gives an explicit parameterized probability density $p_\theta(x)$ via the change-of-variables:

$$\log p_\theta(x) = \log p_Z(f_\theta(x)) + \log |f'_\theta(x)|, \quad (1)$$

where $f'_\theta(x) \in \mathbb{R}^{n \times n}$ is the Jacobian matrix of $f_\theta(x)$ with respect to x , evaluated at x ; $|f'_\theta(x)|$ is its absolute determinant. The distribution of latent codes $p_Z(z)$ is chosen such that the log-density is easy to evaluate and it is easy to sample from. Normalizing flows can be trained by minimizing the negative log-likelihood over the training data:

$$\min_{\theta} \mathcal{L}_{\text{NLL}} = \min_{\theta} \mathbb{E}_{x \sim p_{\text{data}}} [\log p_\theta(x)]. \quad (2)$$

This is equivalent to minimizing the Kullback-Leibler divergence between the true data distribution and the parameterized distribution $\text{KL}(p_{\text{data}} \| p_\theta)$. Sampling from the model is achieved by pushing samples from the latent distribution $z \sim p_Z$ through the inverse of the learned function: $x = f_\theta^{-1}(z) \sim p_\theta(x)$.

Free-form flows (FFF, [11]) soften the restriction that the learned model be invertible. Instead, they learn two separate networks, an encoder f_θ and a decoder g_ϕ coupled by a reconstruction loss:

$$\mathcal{L}_R = \mathbb{E}_{q(x)} [\|g_\phi(f_\theta(x)) - x\|^2]. \quad (3)$$

Encoder and decoder replace f_θ respectively its inverse f_θ^{-1} of an invertible neural network.

Typical normalizing flow architectures are optimized to allow efficient computation of the change of variables term $\log |f'_\theta(x)|$. This usually goes hand in hand with a constrained architecture that is analytically and practically invertible. Free-form flows are based on arbitrary neural networks and the assumption of a tractable change of variables does not hold in general. FFFs therefore estimate the *gradient* of the change of variables via the gradient trick proposed by [46]:

$$\nabla_\theta \mathcal{L}_{\text{NLL}} = \nabla_\theta \mathbb{E}_{q(x)} [-\log p_Z(z) - \text{tr}(f'_\theta(x) \text{SG}[g'_\phi(z)])] \quad (4)$$

$$= \nabla_\theta \mathbb{E}_{x,v} [-\log p_Z(z) - v^T f'_\theta(x) \text{SG}[g'_\phi(z)v]] \quad (5)$$

Here, $z = f_\theta(x)$, $v \in \mathbb{R}^n$ is a random vector with unit covariance, and SG (stop-grad) ensures that gradients only flow to the encoder parameters θ . Instead of $\mathcal{O}(n)$ automatic differentiation steps to compute the full Jacobian $f'_\theta(x)$, this estimator only requires a single vector-Jacobian and a Jacobian-vector product, each of which require one automatic differentiation operation. Note that while the gradient in Eq. (5) is meaningful, the value of \mathcal{L}_{NLL} is not.

Together, this gives the loss of free-form flows with β , the reconstruction weight as a hyperparameter:

$$\mathcal{L}_{\text{FFF}} = \mathcal{L}_{\text{NLL}} + \beta \mathcal{L}_R. \quad (6)$$

In Sec. 4, we demonstrate how this loss can be used to estimate the gradient of the change of variables formula on manifolds, which we now come to.

3.2. Riemannian manifolds

A manifold is a fundamental concept in mathematics, providing a framework for describing and analyzing spaces that locally resemble Euclidean space, but may have different global structure. For example, a small region on a sphere is similar to Euclidean space, but walking in a straight line on the sphere in any direction will return back to the starting point, unlike in Euclidean space.

Mathematically, an n -dimensional manifold, denoted as \mathcal{M} , is a space where every point has a neighborhood that is topologically equivalent to \mathbb{R}^n . A Riemannian manifold (\mathcal{M}, G) extends the concept of a manifold by adding a Riemannian metric G which introduces a notion of distances

and angles. At each point x on the manifold, there is an associated tangent space $\mathcal{T}_x \mathcal{M}$ which is an n -dimensional Euclidean space, characterizing the directions in which you can travel and still stay on the manifold. The metric G acts in this space, defining an inner product between vectors. From this inner product, we can compute the length of paths along the manifold and hence distances between two points.

In this paper, we consider Riemannian manifolds globally embedded into an m -dimensional Euclidean space \mathbb{R}^m , with $n \leq m$. Embedding means that we represent a point on the manifold $x \in \mathcal{M}$ as a vector in \mathbb{R}^m confined to an n -dimensional subspace. A global embedding is a smooth, injective mapping of the entire manifold into a \mathbb{R}^m , its smoothness preserving the topology.

We only work with isometrically embedded manifolds, meaning that the metric is inherited from the ambient Euclidean space. Intuitively, this means that the length of a path on the manifold is just the Euclidean length of that path. We note that due to the Nash embedding theorem [36], every Riemannian manifold has a smooth isometric embedding into Euclidean space of some finite dimension, so in this sense using isometric embeddings is not a limitation. Nevertheless, for some manifolds (especially with negative curvature, e.g. hyperbolic space) there may not be a sensible isometric embedding. We provide a generalization of our method to such manifolds in Sec. 7.2 but do not pursue it experimentally. In Tab. 2, we list the manifolds considered in this paper, their dimension, embedding and how to project from the embedding space to the manifold.

3.3. Change of variables on manifolds

Let (\mathcal{M}_X, G_X) and (\mathcal{M}_Z, G_Z) be n -dimensional Riemannian manifolds. Let $f : \mathcal{M}_X \rightarrow \mathcal{M}_Z$. Then the probability density induced by changing variables with f is

$$\log p_X(x) = \log p_Z(f(x)) + \log |f'(x)| + \frac{1}{2} \log \frac{|G_Z(f(x))|}{|G_X(x)|} \quad (7)$$

with $f'(x)$ the Jacobian of f at x and $|\cdot|$ the absolute determinant. Some care has to be taken with the determinant. Strictly speaking, f' is a linear map between $\mathcal{T}_x \mathcal{M}_X$ and $\mathcal{T}_{f(x)} \mathcal{M}_Z$ and the determinant should be evaluated in those spaces, as visualized in Fig. 2. Naively evaluating in \mathbb{R}^m will give zero if $n < m$: see Sec. 7.1 for a more rigorous treatment and a derivation of Eq. (7).

For the remainder of this paper, we will drop the index on the manifolds \mathcal{M}_X and \mathcal{M}_Z and simply write \mathcal{M} . We do this to simplify notation, but also we use $\mathcal{M}_X = \mathcal{M}_Z$ in all cases. Note that our method easily generalizes to using different manifolds in data and latent space, as long as they are topologically equivalent.

Along with the simplification that the manifolds are iso-

Manifold	Dimension n	Embedding	Projection
Rotations $SO(d)$	$(d-1)d/2$	$\{Q \in \mathbb{R}^{d \times d} : QQ^T = I, \det Q = 1\}$	$R \mapsto \arg \min_{Q \in SO(d)} \ Q - R\ _F$; see Eq. (20)
Sphere \mathbb{S}^n	n	$\{x \in \mathbb{R}^{n+1} : \ x\ = 1\}$	$x \mapsto x/\ x\ $
Torus $\mathbb{T}^n = (\mathbb{S}^1)^n$	n	$\{X \in \mathbb{R}^{n \times 2} : \ X_i\ = 1 \text{ for } i = 1 \dots n\}$	$X_i \mapsto X_i/\ X_i\ $ for $i = 1 \dots n$

Table 2. Manifolds, a global embedding and corresponding projections considered in this paper.

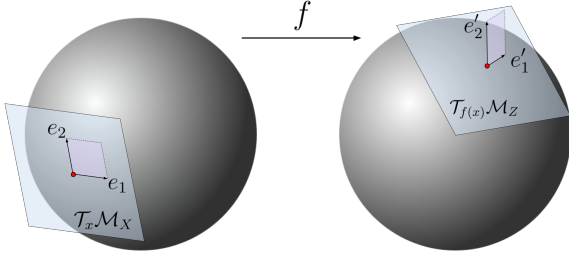


Figure 2. Changing variables between manifolds requires calculations in the tangent spaces of \mathcal{M}_X and \mathcal{M}_Z . Specifically, when changing variables from x to $f(x)$, we need to account for the volume change of the transformation between $\mathcal{T}_x \mathcal{M}_X$ and $\mathcal{T}_{f(x)} \mathcal{M}_Z$. Consider a basis $\{e_i\}$ for the tangent space at x . This basis is transformed under f into $\{e'_i\}$ where $e'_i = f'(x)e_i$. The volume change is the ratio between the areas of the parallelograms (purple regions) formed by e_i and e'_i , equal to the determinant of $f'(x)$, with an additional factor if the manifold is not isometrically embedded, see Sec. 7.1 for details.

metrically embedded, meaning $|G_X| = |G_Z| = 1$, we have

$$\log p_X(x) = \log p_Z(f(x)) + \log |f'(x)|, \quad (8)$$

which is identical to the familiar change of variables formula used in normalizing flows, with the determinant being evaluated in the tangent spaces.

4. Manifold free-form flows

The free-form flow (FFF) framework allows training any pair of parameterized encoder $f_\theta(x)$ and decoder $g_\phi(z)$ as a generative model [11], see Sec. 3.1. In this section, we first show how we set up our models to learn encoders and decoders that are restricted to the manifold. Then, we proceed to show how we adapt the FFF training to manifold free-form flows (M-FFF).

4.1. Learning a function on the manifold

For both encoder f_θ and decoder g_ϕ , we employ feed-forward neural networks $\tilde{f}_\theta, \tilde{g}_\phi : \mathbb{R}^m \rightarrow \mathbb{R}^m$ that act on the embedding space \mathbb{R}^m of the manifold \mathcal{M} . Since the data and latent codes both lie on the manifold, we project the outputs of the networks to the closest point on the man-

ifold:

$$f_\theta(x) = \text{proj}(\tilde{f}_\theta(x)), \quad (9)$$

$$g_\phi(z) = \text{proj}(\tilde{g}_\phi(z)). \quad (10)$$

By restricting the input of both networks to the manifold, we obtain functions acting on the manifold:

$$f_\theta(x) : \mathcal{M} \rightarrow \mathcal{M}, \quad (11)$$

$$g_\phi(z) : \mathcal{M} \rightarrow \mathcal{M}. \quad (12)$$

Figure 1 shows an example that maps from a latent uniform distribution to a bimodal distribution on the circle. In the next section, we explain how to estimate the gradient of the negative log-likelihood.

4.2. Manifold gradient estimator

The adaptation of free-form flows to isometrically embedded manifolds is remarkably simple. Due to the similarity of the change of variables formula (Eq. (8)) to the Euclidean case, we can simply adapt the FFF estimator:

$$\nabla_\theta \mathcal{L}_{\text{NLL}} = \nabla_\theta \mathbb{E}_{x,v} [-\log p_Z(z) - v^T f'_\theta(x) \text{SG}[g'_\phi(z)v]] \quad (13)$$

where the only change is that v must be sampled from the tangent space at $f_\theta(x)$, and must have unit covariance in that space. We achieve this by sampling standard normal vectors $\tilde{v} \in \mathbb{R}^m$ and then projecting them into the tangent space using the Jacobian of the projection function:

$$v = \text{proj}'(f_\theta(x))\tilde{v}. \quad (14)$$

We derive this estimator in detail in Sec. 7.2.

An equivalent formulation is to prepend \tilde{f} and \tilde{g} by a projection in addition to appending the projection:

$$f_\theta = \text{proj} \circ \tilde{f}_\theta \circ \text{proj} \quad (15)$$

and

$$g_\phi = \text{proj} \circ \tilde{g}_\phi \circ \text{proj}. \quad (16)$$

In this case v can be directly sampled in \mathbb{R}^m , so that the Euclidean gradient estimator from Eq. (5) applies without modification. Nevertheless, we choose to use the first formulation (v projected to the tangent space) as it allows us to reduce the variance of the estimate by normalizing v after projection. A discussion of this point can be found in Sec. 7.3.

4.3. Reconstruction loss and other regularization

The reconstruction loss (Eq. (3)) can be modified to use an on-manifold distance (e.g. great circle distance for the sphere) but we find that ambient Euclidean distance works well in practice, since it is almost identical for small distances. Hence we use the same Euclidean reconstruction loss as in free-form flows.

We find that adding the following two regularizations to the loss improve the stability and performance of our models. Firstly, the reconstruction loss on points sampled uniformly from the data manifold:

$$\mathcal{L}_U = \mathbb{E}_{x \sim \mathcal{U}(\mathcal{M})} [\|g_\phi(f_\theta(x)) - x\|^2] \quad (17)$$

which helps ensure that we have a globally consistent mapping between the data and latent manifolds in low data regions. Secondly, the squared distance between the output of f_θ and its projection to the manifold:

$$\mathcal{L}_P = \mathbb{E}_{q(x)} [\|\tilde{f}_\theta(x) - f_\theta(x)\|^2] \quad (18)$$

which discourages the output of \tilde{f}_θ from entering unprojectable regions, for example the origin when the manifold is \mathbb{S}^n . The same regularizations can be applied starting from the latent space.

The full loss is:

$$\mathcal{L} = \mathcal{L}_{\text{NLL}} + \beta_R \mathcal{L}_R + \beta_U \mathcal{L}_U + \beta_P \mathcal{L}_P \quad (19)$$

where β_R , β_U and β_P are hyperparameters. We give our choices in Sec. 8.

5. Experiments

In this section, we demonstrate the practical performance of manifold free-form flows on a variety of manifolds. We choose established experiments to ensure comparability with previous methods. Generally, we find that we obtain competitive performance with the advantage that our method samples orders of magnitudes faster because it requires only a single function evaluation. In contrast, previous general purpose work integrates a differential equation on the manifold, which requires multiple model evaluations.

We give all details on training in the appendix.

5.1. Synthetic distribution over rotation matrices

The group of 3D rotations $SO(3)$ can be represented by rotations matrices with positive determinant, i.e. all $Q \in \mathbb{R}^{3 \times 3}$ with $Q^T Q = I$ and $\det Q = 1$. To apply manifold free-form flows, we project an output matrix $R \in \mathbb{R}^{3 \times 3}$ from the encoder/decoder to the subspace of special orthogonal matrices by finding the matrix $Q \in SO(3)$ minimizing the Frobenius norm $\|Q - R\|_F$. This is known as the

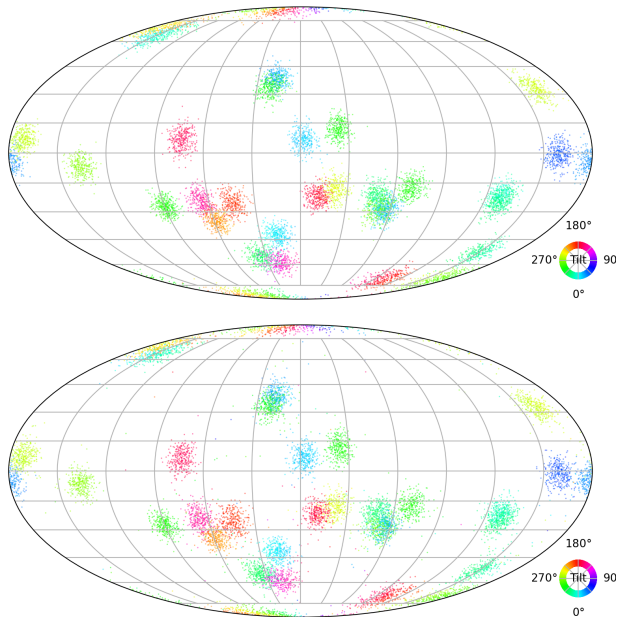


Figure 3. Manifold free-form flows on a synthetic $SO(3)$ mixture distribution with $M = 64$ mixture components proposed by [10]. (Top) 10,000 samples each from the ground truth distribution and (bottom) our model. This visualization computes three Euler angles, which fully describe a rotation matrix, and then plot the first two angles on the projection of a sphere and the last by color [34]. We find that our model nicely samples from the distribution with few outliers between the modes.

constrained Procrustes problem and the solution Q can be determined via the SVD $R = U \Sigma V^T$ [26]:

$$Q = U S V^T, \quad (20)$$

where the diagonal entries of Σ were sorted from largest to smallest and $S = \text{Diag}(1, \dots, 1, \det(UV^T))$.

We learn a M-FFF on synthetic mixture distributions proposed by [10] with M mixture components for $M = 16, 32$ and 64 . Samples from one of the distributions and samples from our model are depicted in Fig. 3.

M-FFF achieves negative log-likelihoods on par or better than previous methods, see Tab. 3. At the same time, it speeds up sampling by about two orders of magnitude since it requires only a single function evaluation to sample.

5.2. Earth data on the sphere

We evaluate manifold free-form flows on spheres with datasets from the domain of earth sciences. We use four established datasets compiled by [30] for density estimation on \mathbb{S}^2 : Volcanic eruptions [38], earthquakes [37], floods [4] and wildfires [12].

We compare M-FFF to Riemannian score-based generative models [10], Riemannian diffusion models [20], Riemannian flow matching [8] and the other baseline models

	$M = 16$	$M = 32$	$M = 64$	Sampling steps
Moser flow [45]	-0.85 ± 0.03	-0.17 ± 0.03	0.49 ± 0.02	~ 1000
Exp-wrapped SGM [10]	-0.87 ± 0.04	-0.16 ± 0.03	0.58 ± 0.04	~ 500
Riemannian SGM [10]	-0.89 ± 0.03	-0.20 ± 0.03	0.49 ± 0.02	~ 100
M-FFF (ours)	-0.87 ± 0.02	-0.21 ± 0.02	0.45 ± 0.02	1

Table 3. Results on synthetic $SO(3)$ mixtures. We compare the final model’s negative log-likelihood (NLL, \downarrow) and the number of function evaluations necessary to obtain a single sample averaged over five runs \pm standard deviations. Our manifold free-form flows (M-FFF) achieve comparable likelihoods at greatly improved sampling speed. Baselines values due to [10].

	Volcano	Earthquake	Flood	Fire	Sampling steps
Mixture of Kent [41]	-0.80 ± 0.47	0.33 ± 0.05	0.73 ± 0.07	-1.18 ± 0.06	N/A
Riemannian CNF [30]	-6.05 ± 0.61	0.14 ± 0.23	1.11 ± 0.19	-0.80 ± 0.54	~ 100
Moser flow [45]	-4.21 ± 0.17	-0.16 ± 0.06	0.57 ± 0.10	-1.28 ± 0.05	~ 100
Stereographic score-based [10]	-3.80 ± 0.27	-0.19 ± 0.05	0.59 ± 0.07	-1.28 ± 0.12	~ 100
Riemannian score-based [10]	-4.92 ± 0.25	-0.19 ± 0.07	0.45 ± 0.17	-1.33 ± 0.06	~ 100
Riemannian diffusion [20]	-6.61 ± 0.97	-0.40 ± 0.05	0.43 ± 0.07	-1.38 ± 0.05	> 100
Riemannian flow matching [8]	-7.93 ± 1.67	-0.28 ± 0.08	0.42 ± 0.05	-1.86 ± 0.11	not reported
M-FFF (ours)	-2.25 ± 0.02	-0.23 ± 0.01	0.51 ± 0.01	-1.19 ± 0.03	1

Table 4. Negative log-likelihoods for the earth datasets (lower is better). Results for the baselines taken from [10], [20] and [8]. While our results show mixed performance compared to the baselines, we uniquely provide a competitive single-step sampling method.

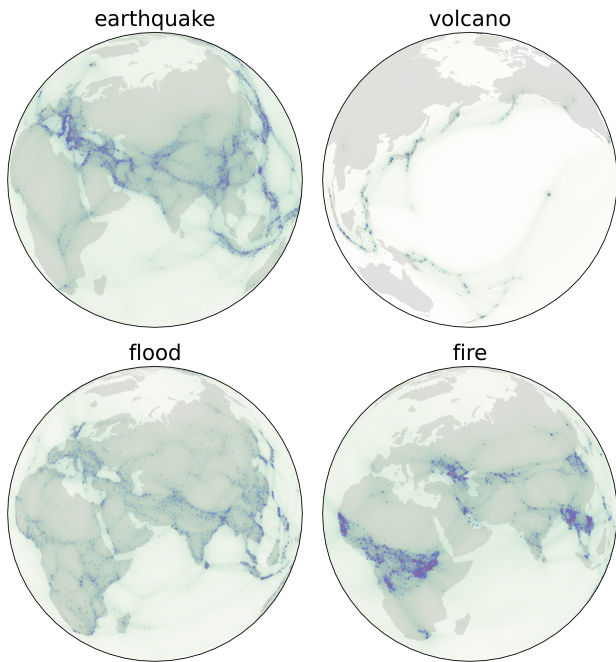


Figure 4. Density estimates of our model on the earth datasets. Blue points show the training dataset, red points the test dataset.

used in [10]. We provide a full comparison of negative log-likelihoods in Table 4 and visualize the learned densities in Figure 4. Our method has a mixed performance, but provides the only competitive solution that allows for single-step sampling. While it is outperformed by Rie-

mannian flow matching in all datasets, the computational cost of training and evaluation is significantly smaller due to the single step sampling and greatly reduced model size (around 100 times smaller).

We notice that, since there are many regions without training data in the different datasets, the predicted latent codes and thus likelihood estimates of the validation set are often inaccurate. To ensure an accurate estimation of the data likelihood under the decoder, during evaluation we sample multiple latent points $z \sim \mathcal{N}(f_\theta(x), 10^{-4})$ from a small region around the predicted latent point and project them back onto the manifold. To estimate the likelihood of x we pick the point $z^* = \arg \min_z d(x, g_\phi(z))$. This results in a reduction of the reconstruction error from 80km to less than 10km on average. We find that the likelihoods computed in this way now agree with the decoder distribution. Note that this does not affect sampling speed.

5.3. Torsion angles of molecules on tori

To benchmark manifold free-form flows on tori \mathbb{T}^n , we follow [20] and evaluate our model on two datasets from structural biology. We consider the torsion (dihedral) angles of the backbone of protein and RNA substructures respectively.

We represent a tuple of angles $(\phi_1, \dots, \phi_n) \in [0, 2\pi]^n$ by mapping each angle to a position on a circle: $X_i = (\cos \phi_i, \sin \phi_i) \in \mathbb{S}^1$. Then we stack all X_i into a matrix $X \in \mathbb{R}^{n \times 2}$, compare Tab. 2.

The first dataset is comprised of 500 proteins assembled by [29] and is located on \mathbb{T}^2 . The three dimensional ar-

	General	Glycine	Proline	Pre-Pro	RNA	Sampling steps
Mixture of power spherical [20]	1.15 ± 0.002	2.08 ± 0.009	0.27 ± 0.008	1.34 ± 0.019	4.08 ± 0.368	N/A
Riemannian diffusion models [20]	1.04 ± 0.012	1.97 ± 0.012	0.12 ± 0.011	1.24 ± 0.004	-3.70 ± 0.592	~ 1000
Riemannian flow matching [8]	1.01 ± 0.025	1.90 ± 0.055	0.15 ± 0.027	1.18 ± 0.055	-5.20 ± 0.067	not reported
M-FFF (ours)	1.03 ± 0.0002	1.92 ± 0.0013	0.21 ± 0.0019	1.27 ± 0.004	-4.27 ± 0.09	1

Table 5. Negative log-likelihoods (NLL, \downarrow) on torus datasets. Experimental data for a mixture of 4096 power spherical distributions [7] and Riemannian diffusion models are taken from [20]. Furthermore, we compare against Riemannian flow matching [8]. Mean and standard deviation are evaluated over five independent models for each dataset. Notably, our method is able to achieve on par negative log-likelihoods with a single sampling step on most of the datasets and even outperforms Riemannian diffusion models on some of them.

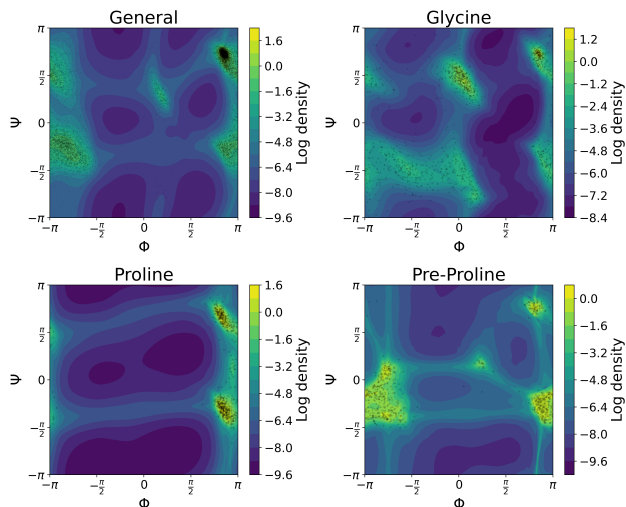


Figure 5. Log density of M-FFF models in the (Φ, Ψ) -plane of protein backbone dihedral angles. The test data for each dataset is shown as black dots. This representation was introduced by [42] and is known as Ramachandran plot. Note how the learned distribution adheres to the periodic boundary conditions.

range of a protein backbone can be described by the so called Ramachandran angles [42] Φ and Ψ , which represent the torsion of the backbone around the $N - C_\alpha$ and $C_\alpha - C$ bonds. The data is split into four distinct subsets *General*, *Glycine*, *Proline* and *Pre-Proline*, depending on the residue of each substructure.

The second dataset is extracted from a subset of RNA structures introduced by [35]. As the RNA backbone structure can be characterized by seven torsion angles, in this case we are dealing with data on \mathbb{T}^7 .

We record the negative log-likelihoods of our method in Tab. 5 and compare it to previous approaches. Notably, our approach demonstrates comparable performance across all datasets at fast sampling speed. In addition to the quantitative results, in Fig. 5 we show the log densities of the M-FFF models for the four protein datasets.

6. Conclusion

In this paper, we present manifold free-form flows (M-FFF) to learn a probability distribution on a manifold. They are based on a neural network construction that learns a function in an embedding space whose outputs are projected to the manifold (Fig. 1). This naturally makes the learned distributions adhere to the topology of the manifold at hand.

The distribution on the manifold is then learned by adapting the framework of free-form flows (FFF) to manifolds. We extend it to estimate the gradient of the change of variables formula for manifold-to-manifold functions.

The main advantage of M-FFF is that they offer competitive performance similar to previous ODE- or SDE-based methods at greatly reduced sampling costs, typically between two and three orders of magnitude faster. In addition, they are very easy to set up, since only a projection from the embedding space to the manifold needs to be known.

Acknowledgements

This work is supported by Deutsche Forschungsgemeinschaft (DFG, German Research Foundation) under Germany’s Excellence Strategy EXC-2181/1 - 390900948 (the Heidelberg STRUCTURES Cluster of Excellence). It is also supported by the Vector Stiftung in the project TRINN (P2019-0092), and by Informatics for Life funded by the Klaus Tschira Foundation. AR acknowledges funding from the Carl-Zeiss-Stiftung. The authors acknowledge support by the state of Baden-Württemberg through bwHPC and the German Research Foundation (DFG) through grant INST 35/1597-1 FUGG.

References

- [1] Heli Ben-Hamu, Samuel Cohen, Joey Bose, Brandon Amos, Maximillian Nickel, Aditya Grover, Ricky TQ Chen, and Yaron Lipman. Matching normalizing flows and probability paths on manifolds. In *International Conference on Machine Learning*, pages 1749–1763. PMLR, 2022. 2
- [2] Joey Bose, Ariella Smofsky, Renjie Liao, Prakash Panangaden, and Will Hamilton. Latent variable modelling with hyperbolic normalizing flows. In *International Conference on Machine Learning*, pages 1045–1055. PMLR, 2020. 2

- [3] Denis Boyda, Gurtej Kanwar, Sébastien Racanière, Danilo Jimenez Rezende, Michael S. Albergo, Kyle Cranmer, Daniel C. Hackett, and Phiala E. Shanahan. Sampling using $SU(n)$ gauge equivariant flows. *Phys. Rev. D*, 103: 074504, 2021. [2](#)
- [4] G Brakenridge. Global active archive of large flood events. <http://floodobservatory.colorado.edu/Archives/index.html>, 2017. [5](#)
- [5] James A Brofos, Marcus A Brubaker, and Roy R Lederman. Manifold density estimation via generalized dequantization. *arXiv preprint arXiv:2102.07143*, 2021. [2](#)
- [6] Tom Brown, Benjamin Mann, Nick Ryder, Melanie Subbiah, Jared D Kaplan, Prafulla Dhariwal, Arvind Neelakantan, Pranav Shyam, Girish Sastry, Amanda Askell, et al. Language models are few-shot learners. *Advances in neural information processing systems*, 33:1877–1901, 2020. [1](#)
- [7] Nicola De Cao and Wilker Aziz. The power spherical distribution, 2020. [7](#)
- [8] Ricky TQ Chen and Yaron Lipman. Riemannian flow matching on general geometries. *arXiv preprint arXiv:2302.03660*, 2023. [1](#), [2](#), [5](#), [6](#), [7](#)
- [9] Tim R. Davidson, Luca Falorsi, Nicola De Cao, Thomas Kipf, and Jakub M. Tomczak. Hyperspherical variational auto-encoders. *34th Conference on Uncertainty in Artificial Intelligence (UAI-18)*, 2018. [15](#)
- [10] Valentin De Bortoli, Emile Mathieu, Michael Hutchinson, James Thornton, Yee Whye Teh, and Arnaud Doucet. Riemannian score-based generative modelling. *Advances in Neural Information Processing Systems*, 35:2406–2422, 2022. [1](#), [2](#), [5](#), [6](#), [14](#)
- [11] Felix Draxler, Peter Sorrenson, Lea Zimmermann, Armand Rousselot, and Ullrich Köthe. Free-form flows: Make any architecture a normalizing flow. *arXiv preprint arXiv:2310.16624*, 2023. [1](#), [2](#), [3](#), [4](#)
- [12] EOSDIS. Land, atmosphere near real-time capability for eos (lance) system operated by nasa’s earth science data and information system (esdis). <https://earthdata.nasa.gov/earth-observation-data/near-real-time/firms/active-fire-data>, 2020. [5](#)
- [13] William Falcon and The PyTorch Lightning team. PyTorch lightning, 2019. [15](#)
- [14] Luca Falorsi. Continuous normalizing flows on manifolds. *arXiv preprint arXiv:2104.14959*, 2021. [2](#)
- [15] Luca Falorsi and Patrick Forré. Neural ordinary differential equations on manifolds. *arXiv preprint arXiv:2006.06663*, 2020. [2](#)
- [16] Luca Falorsi, Pim de Haan, Tim R Davidson, and Patrick Forré. Reparameterizing distributions on lie groups. In *The 22nd International Conference on Artificial Intelligence and Statistics*, pages 3244–3253. PMLR, 2019. [2](#)
- [17] Mevlana C Gemic, Danilo Rezende, and Shakir Mohamed. Normalizing flows on riemannian manifolds. *arXiv preprint arXiv:1611.02304*, 2016. [2](#)
- [18] A Girard. A fast ‘Monte-Carlo cross-validation’ procedure for large least squares problems with noisy data. *Numerische Mathematik*, 56:1–23, 1989. [13](#)
- [19] Charles R. Harris, K. Jarrod Millman, Stéfan J. van der Walt, Ralf Gommers, Pauli Virtanen, David Cournapeau, Eric Wieser, Julian Taylor, Sebastian Berg, Nathaniel J. Smith, Robert Kern, Matti Picus, Stephan Hoyer, Marten H. van Kerkwijk, Matthew Brett, Allan Haldane, Jaime Fernández del Río, Mark Wiebe, Pearu Peterson, Pierre Gérard-Marchant, Kevin Sheppard, Tyler Reddy, Warren Weckesser, Hameer Abbasi, Christoph Gohlke, and Travis E. Oliphant. Array programming with NumPy. *Nature*, 585(7825):357–362, 2020. [15](#)
- [20] Chin-Wei Huang, Milad Aghajohari, Joey Bose, Prakash Panangaden, and Aaron C Courville. Riemannian diffusion models. *Advances in Neural Information Processing Systems*, 35:2750–2761, 2022. [1](#), [2](#), [5](#), [6](#), [7](#)
- [21] J. D. Hunter. Matplotlib: A 2D graphics environment. *Computing in Science & Engineering*, 9(3):90–95, 2007. [15](#)
- [22] Jürgen Jost. *Riemannian geometry and geometric analysis*. Springer, 2008. [10](#)
- [23] Dimitris Kalatzis, Johan Ziruo Ye, Alison Pouplin, Jesper Wohlert, and Søren Hauberg. Density estimation on smooth manifolds with normalizing flows. *arXiv preprint arXiv:2106.03500*, 2021. [2](#)
- [24] Gurtej Kanwar, Michael S. Albergo, Denis Boyda, Kyle Cranmer, Daniel C. Hackett, Sébastien Racanière, Danilo Jimenez Rezende, and Phiala E. Shanahan. Equivariant flow-based sampling for lattice gauge theory. *Physical Review Letters*, 125(12), 2020. [2](#)
- [25] Lars Erik Kühmichel and Felix Draxler. Lightning trainable, 2023. [15](#)
- [26] Jim Lawrence, Javier Bernal, and Christoph Witzgall. A purely algebraic justification of the kabsch-umeyama algorithm. *Journal of research of the National Institute of Standards and Technology*, 124:1, 2019. [5](#)
- [27] Yulin Liu, Haoran Liu, Yingda Yin, Yang Wang, Baoquan Chen, and He Wang. Delving into discrete normalizing flows on so (3) manifold for probabilistic rotation modeling. In *Proceedings of the IEEE/CVF Conference on Computer Vision and Pattern Recognition*, pages 21264–21273, 2023. [2](#)
- [28] Aaron Lou, Derek Lim, Isay Katsman, Leo Huang, Qingxuan Jiang, Ser Nam Lim, and Christopher M De Sa. Neural manifold ordinary differential equations. *Advances in Neural Information Processing Systems*, 33:17548–17558, 2020. [2](#)
- [29] Simon C. Lovell, Ian W. Davis, W. Bryan Arendall III, Paul I. W. de Bakker, J. Michael Word, Michael G. Prisant, Jane S. Richardson, and David C. Richardson. Structure validation by α geometry: ϕ, ψ and $c\beta$ deviation. *Proteins: Structure, Function, and Bioinformatics*, 50(3):437–450, 2003. [6](#)
- [30] Emile Mathieu and Maximilian Nickel. Riemannian continuous normalizing flows. *Advances in Neural Information Processing Systems*, 33:2503–2515, 2020. [1](#), [2](#), [5](#), [6](#)
- [31] Wes McKinney. Data Structures for Statistical Computing in Python. In *9th Python in Science Conference*, 2010. [15](#)
- [32] Nina Miolane, Nicolas Guigui, Alice Le Brigant, Johan Mathe, Benjamin Hou, Yann Thanwerdas, Stefan Heyder, Olivier Peltre, Niklas Koep, Hadi Zaatiti, Hatem Hajri, Yann Cabanes, Thomas Gerald, Paul Chauchat, Christian Shewmake, Daniel Brooks, Bernhard Kainz, Claire Donnat, Susan

- Holmes, and Xavier Pennec. Geomstats: A python package for riemannian geometry in machine learning. *Journal of Machine Learning Research*, 21(223):1–9, 2020. 15
- [33] Nina Miolane, Saiteja Utpala, Nicolas Guigui, Luís F. Pereira, Alice Le Brigant, Hzaatiti, Yann Cabanes, Johan Mathe, Niklas Koep, elodiemaignant, ythanwerdas, xpenec, tgeral68, Christian, Tra My Nguyen, Olivier Peltre, pchauchat, Jules-Deschamps, John Harvey, mortenapederesen, Maya95assal, Quentin Barthélemy, Abdellaoui-Souhail, Adele Myers, Felix Ambellan, Florent-Michel, Shubham Talbar, Stefan Heyder, Yann de Mont-Marin, and Marius. geomstats/geomstats: Geomstats v2.7.0, 2023. 15
- [34] Kieran A Murphy, Carlos Esteves, Varun Jampani, Srikanth Ramalingam, and Ameesh Makadia. Implicit-pdf: Non-parametric representation of probability distributions on the rotation manifold. In *International Conference on Machine Learning*, pages 7882–7893. PMLR, 2021. 5
- [35] Laura Murray, W Arendall, David Richardson, and Jane Richardson. Rna backbone is rotameric. *Proceedings of the National Academy of Sciences of the United States of America*, 100:13904–9, 2003. 7
- [36] John Nash. The imbedding problem for riemannian manifolds. *Annals of mathematics*, 63(1):20–63, 1956. 3
- [37] National Geophysical Data Center / World Data Service (NGDC/WDS). Ncei/wds global significant earthquake database. <https://www.ncei.noaa.gov/access/metadata/landing-page/bin/iso?id=gov.noaa.ngdc.mgg.hazards:G012153>, 2022. 5
- [38] National Geophysical Data Center / World Data Service (NGDC/WDS). Ncei/wds global significant volcanic eruptions database. <https://www.ncei.noaa.gov/access/metadata/landing-page/bin/iso?id=gov.noaa.ngdc.mgg.hazards:G10147>, 2022. 5
- [39] Frank Noé, Simon Olsson, Jonas Köhler, and Hao Wu. Boltzmann generators: Sampling equilibrium states of many-body systems with deep learning. *Science*, 365(6457): eaaw1147, 2019. 1
- [40] Adam Paszke, Sam Gross, Francisco Massa, Adam Lerer, James Bradbury, Gregory Chanan, Trevor Killeen, Zeming Lin, Natalia Gimelshein, Luca Antiga, et al. Pytorch: An imperative style, high-performance deep learning library. *Advances in neural information processing systems*, 32, 2019. 15
- [41] David Peel, William J Whiten, and Geoffrey J McLachlan. Fitting mixtures of kent distributions to aid in joint set identification. *Journal of the American Statistical Association*, 96(453):56–63, 2001. 6
- [42] G. N. Ramachandran, C. Ramakrishnan, and V. Sasisekharan. Stereochemistry of polypeptide chain configurations. *Journal of Molecular Biology*, 7(1):95–99, 1963. 7
- [43] Danilo Jimenez Rezende, George Papamakarios, Sébastien Racaniere, Michael Albergo, Gurtej Kanwar, Phiala Shanahan, and Kyle Cranmer. Normalizing flows on tori and spheres. In *International Conference on Machine Learning*, pages 8083–8092. PMLR, 2020. 2
- [44] Robin Rombach, Andreas Blattmann, Dominik Lorenz, Patrick Esser, and Björn Ommer. High-resolution image synthesis with latent diffusion models. In *Proceedings of the IEEE/CVF Conference on Computer Vision and Pattern Recognition*, pages 10684–10695, 2022. 1
- [45] Noam Rozen, Aditya Grover, Maximilian Nickel, and Yaron Lipman. Moser flow: Divergence-based generative modeling on manifolds. *Advances in Neural Information Processing Systems*, 34:17669–17680, 2021. 1, 2, 6
- [46] Peter Sorrenson, Felix Draxler, Armand Rousselot, Sander Hummerich, Lea Zimmermann, and Ullrich Köthe. Lifting architectural constraints of injective flows. *arXiv:2306.01843*, 2023. 2, 3
- [47] The pandas development team. Pandas-dev/pandas: Pandas, 2020. 15

Learning Distributions on Manifolds with Free-form Flows

Supplementary Material

7. Free-form flows on Riemannian manifolds

In this appendix, we will focus on intuitive definitions of concepts from topology and differential geometry. For a more rigorous treatment of these concepts, see [22].

An n -dimensional manifold \mathcal{M} is a space where every point x has a neighborhood which is homeomorphic to an open subset of \mathbb{R}^n . Intuitively, this means that there is a small region of \mathcal{M} containing x which can be bent and stretched in a continuous way to map onto a small region in \mathbb{R}^n . This is what is meant when we say that the manifold locally resembles \mathbb{R}^n . If all these maps from \mathcal{M} to \mathbb{R}^n are also differentiable then the manifold itself is differentiable, as long as there is a way to connect up the local neighborhoods in a differentiable and consistent way.

The tangent space of the manifold at x , denoted $\mathcal{T}_x\mathcal{M}$, is an n -dimensional Euclidean space, which is a linearization of the manifold at x : if we zoom in to a very small region around x the manifold looks flat, and this flat Euclidean space is aligned with the tangent space. Because the tangent space is a linearization of the manifold, this is where derivatives on the manifold live, e.g. if $f : \mathcal{M}_X \rightarrow \mathcal{M}_Z$ is a map between two manifolds, then the Jacobian $f'(x)$ is a linear map from $\mathcal{T}_x\mathcal{M}_X$ to $\mathcal{T}_{f(x)}\mathcal{M}_Z$.

A Riemannian manifold (\mathcal{M}, g) is a differentiable manifold which is equipped with a Riemannian metric $g : \mathcal{T}_x\mathcal{M} \times \mathcal{T}_x\mathcal{M} \rightarrow \mathbb{R}$ which defines an inner product on the tangent space, which allows us to calculate lengths and angles in this space. The length of a smooth curve $\gamma : [0, 1] \rightarrow \mathcal{M}$ is given by the integral of the length of its velocity vector $\gamma'(t) \in \mathcal{T}_{\gamma(t)}\mathcal{M}$. This ultimately allows us to define a notion of distance on the manifold, as the curve of minimal length connecting two points.

In the remainder of the appendix we only consider Riemannian manifolds.

7.1. Manifold change of variables

Embedded manifolds We define an n -dimensional manifold embedded in \mathbb{R}^m via a projection function

$$\text{proj} : P \rightarrow \mathbb{R}^m \quad (21)$$

where $P \subseteq \mathbb{R}^m$ is the projectable set. We require the projection to have the following properties (the first is true of all projections, the others are additional requirements):

1. $\text{proj} \circ \text{proj} = \text{proj}$
2. proj is smooth on P
3. $\text{rank}(\text{proj}'(\text{proj}(x))) = n$ for all $x \in P$

Given such a projection, we define a manifold by

$$\mathcal{M} = \{x \in \mathbb{R}^m : \text{proj}(x) = x\} \quad (22)$$

with the tangent space

$$\mathcal{T}_x\mathcal{M} = \text{col}(\text{proj}'(x)) \quad (23)$$

where col denotes the column space. Since the rank of $\text{proj}'(x)$ with $x \in \mathcal{M}$ is n , the tangent space is n -dimensional and \mathcal{M} is an n -dimensional manifold. The Riemannian metric $g_x : \mathcal{T}_x\mathcal{M} \times \mathcal{T}_x\mathcal{M} \rightarrow \mathbb{R}$ defined on this manifold is realized as an $m \times m$ matrix $G(x)$. If \mathcal{M} is isometrically embedded then $G(x)$ is just the identity matrix.

The Jacobian of the projection is a projection matrix, meaning $\text{proj}'(x)\text{proj}'(x) = \text{proj}'(x)$ for $x \in \mathcal{M}$. For any v in the column space of $\text{proj}'(x)$, there is a u such that $v = \text{proj}'(x)u$ and due to the projection property, $\text{proj}'(x)v = \text{proj}'(x)u = v$. Similarly, for any w in the row space of $\text{proj}'(x)$, $w\text{proj}'(x) = w$. If proj is an orthogonal projection, proj' is symmetric by definition and hence the row and column spaces are identical.

Integration on embedded manifolds In order to perform integration on the manifold, we cannot work directly in the m -dimensional coordinates of the embedding space, instead we have to introduce some local n -dimensional coordinates. This means that the domain of integration has to be diffeomorphic to an open set in \mathbb{R}^n . Since this might not be the case for the whole region of integration, we might need to partition it into such regions and perform integration on each individually (each such region, together with its map to \mathbb{R}^n , is known as a chart and a collection of charts is an atlas). For example, if we want to integrate a function on the sphere, we could split the sphere into two hemispheres and integrate each separately. A hemisphere can be continuously stretched and flattened into a 2-dimensional region, whereas the whole sphere cannot without creating discontinuities.

Given an open set U in \mathbb{R}^n , and a diffeomorphic local embedding function $\phi : U \rightarrow \mathcal{M}$, the integral of a scalar function $p : \mathcal{M} \rightarrow \mathbb{R}$ on $\phi(U) \subseteq \mathcal{M}$ is

$$\int_{\phi(U)} p dV = \int_U (p \circ \phi) \sqrt{|\phi'(u)^T G(\phi(u)) \phi'(u)|} du^1 \cdots du^n \quad (24)$$

where $G(\phi(u))$ is the matrix representation of $g_{\phi(u)}$. The integral on the right is an ordinary integral in \mathbb{R}^n . The quantity inside the determinant is known as the pullback metric.

Theorem 1 (Manifold change of variables). *Let (\mathcal{M}_X, g_X) and (\mathcal{M}_Z, g_Z) be n -dimensional Riemannian manifolds*

embedded in \mathbb{R}^m with the same global topological structure. Let p_X be a probability distribution on \mathcal{M}_X and let $f : \mathcal{M}_X \rightarrow \mathcal{M}_Z$ be a diffeomorphism. Let p_Z be the pushforward of p_X under f (i.e. if p_X is the probability density of X , p_Z is the probability density of $f(X)$).

Let $x \in \mathcal{M}_X$. Let $Q \in \mathbb{R}^{m \times n}$ be an orthonormal basis for $\mathcal{T}_x \mathcal{M}_X$ and $R \in \mathbb{R}^{m \times n}$ an orthonormal basis for $\mathcal{T}_{f(x)} \mathcal{M}_Z$.

Then p_X and p_Z are related under the change of variables $x \mapsto f(x)$ by:

$$\log p_X(x) = \log p_Z(f(x)) + \log |R^T f'(x) Q| + \frac{1}{2} \log \frac{|R^T G_Z(f(x)) R|}{|Q^T G_X(x) Q|}. \quad (25)$$

Note that Q and R depend on x and $f(x)$ respectively, but this is omitted for brevity.

In the main text we state a simplified form of the equation:

$$\log p_X(x) = \log p_Z(f(x)) + \log |f'(x)| + \frac{1}{2} \log \frac{|G_Z(f(x))|}{|G_X(x)|} \quad (26)$$

with the statement that the determinants have to be evaluated in the tangent spaces, not in the ambient m -dimensional space. This is equivalent to the statement of Theorem 1.

Below, we provide two versions of the proof, the second being a less rigorous and more geometric variant of the first.

Proof. Let $\phi : \mathbb{R}^n \rightarrow \mathcal{M}_X$ be defined by $\phi(u) = \text{proj}_X(x + Qu)$. Let U be an open subset of \mathbb{R}^n containing the origin which is small enough so that ϕ is bijective. Let $\psi : \mathbb{R}^n \rightarrow \mathcal{M}_Z$ be defined by $\psi(w) = \text{proj}_Z(f(x) + R w)$. Define $\varphi = \psi^{-1} \circ f \circ \phi$ and let $W = \varphi(U)$.

Note that $\phi'(u) = \text{proj}'_X(x + Qu) \cdot Q$ and hence $\phi'(0) = \text{proj}'_X(x) Q = Q$ (since each column of Q is in $\mathcal{T}_x \mathcal{M}_X = \text{col}(\text{proj}'_X(x))$).

Similarly, $\psi'(0) = R$. Since ψ is a map from n to m dimensions, there is not a unique function from \mathbb{R}^m to \mathbb{R}^n which is ψ^{-1} on the manifold and there are remaining degrees of freedom which can result in different Jacobians. For our purposes, we define the inverse ψ^{-1} such that $\psi \circ \psi^{-1}$ is an orthogonal projection onto \mathcal{M}_Z . This means $\psi'(\psi^{-1}(f(x))) (\psi^{-1})'(f(x)) = R R^T$ and hence $(\psi^{-1})'(f(x)) = R^T$.

Since p_Z is the pushforward of p_X under f , the amount of probability mass contained in $\phi(U)$ is the same as that contained in $f(\phi(U)) = \psi(W)$:

$$\int_{\phi(U)} p_X(x) dV_X = \int_{\psi(W)} p_Z(z) dV_Z \quad (27)$$

and therefore:

$$\begin{aligned} & \int_U p_X(\phi(u)) \sqrt{|Q^T G_X(\phi(u)) Q|} du^1 \dots du^n \\ &= \int_W p_Z(\psi(w)) \sqrt{|R^T G_Z(\psi(w)) R|} dw^1 \dots dw^n. \end{aligned} \quad (28)$$

Note that Q and R also depend on u . Changing variables of the RHS with $w = \varphi(u)$ gives us

$$\begin{aligned} & \int_U p_X(\phi(u)) \sqrt{|Q^T G_X(\phi(u)) Q|} du^1 \dots du^n \\ &= \int_U p_Z(f(\phi(u))) \sqrt{|R^T G_Z(f(\phi(u))) R|} \left| \frac{\partial w}{\partial u} \right| du^1 \dots du^n. \end{aligned} \quad (29)$$

Since U was arbitrary, we can make it arbitrarily small, demonstrating that the integrands must be equal for $u = 0$:

$$\begin{aligned} p_X(x) \sqrt{|Q^T G_X(x) Q|} \\ &= p_Z(f(x)) \sqrt{|R^T G_Z(f(x)) R|} \cdot \left| \frac{\partial w}{\partial u} \right|. \end{aligned} \quad (30)$$

where now Q is evaluated at $u = 0$ and R at $w = \varphi(0)$. Since $w = \psi^{-1}(f(\phi(u)))$, the Jacobian has the following form when evaluated at the origin (note $\phi(0) = x$):

$$\frac{\partial w}{\partial u} = (\psi^{-1})'(f(x)) \cdot f'(x) \cdot \phi'(0) \quad (31)$$

$$= R^T f'(x) Q. \quad (32)$$

Substituting this into the equality, rearranging and taking the logarithm gives the result:

$$\begin{aligned} \log p_X(x) &= \log p_Z(f(x)) + \log |R^T f'(x) Q| \\ &+ \frac{1}{2} \log \frac{|R^T G_Z(f(x)) R|}{|Q^T G_X(x) Q|}. \end{aligned} \quad (33)$$

□

Alternative proof Here is a less rigorous and more geometric proof, which may be more intuitive for some readers.

Proof. Let x be a point on \mathcal{M}_X . Consider a small square region $U \subseteq \mathcal{M}$ around x (hypercube region in higher dimensions). If the sides of the square are small enough, the square is approximately tangent to the manifold since the manifold looks very flat if we zoom in. Suppose Q is a basis for the tangent space at x and q^1, \dots, q^n are the columns of Q . Suppose that the sides of the square (or hypercube) are spanned by $u^i = \epsilon q^i$ for a small ϵ . The volume spanned by a parallelepiped (higher-dimensional analog of a parallelogram) is the square root of the determinant of the Gram matrix of inner products:

$$\text{vol}(u^1, \dots, u^n) = \sqrt{|\langle u^i, u^j \rangle|}. \quad (34)$$

The inner product is given by G , namely $\langle u, v \rangle = u^T G v$. We can therefore write the volume of U as

$$\text{vol}(U) \approx \epsilon^n \sqrt{|Q^T G Q|}. \quad (35)$$

Now consider how U is transformed under f . It will be mapped to a region $f(U)$ on \mathcal{M}_z with approximately straight edges, forming an approximate parallelotope in the tangent space at $z = f(x)$. This region will be spanned by the columns of $f'(x)\epsilon Q$ (since $f(x+u^i) \approx f(x) + f'(x)u^i$) and hence will have a volume of

$$\text{vol}(f(U)) \approx \epsilon^n \sqrt{|Q^T f'(x)^T G_Z(z) f'(x) Q|} \quad (36)$$

$$= \epsilon^n \sqrt{|Q^T f'(x)^T R R^T G_Z(z) R R^T f'(x) Q|} \quad (37)$$

$$= \epsilon^n |R^T f'(x) Q| \sqrt{|R^T G_Z(z) R|} \quad (38)$$

where R is a basis for the tangent space at $f(x)$. We can introduce $R R^T$ into the expression since it is a projection in the tangent space at $f(x)$ and is essentially the identity within that space. Since the RHS of $G_Z(z)$ and the LHS of $f'(x)$ both live in this tangent space, we can introduce $R R^T$ between them without changing the expression. Then in the last step we use that $|AB| = |A||B|$ for square matrices.

Since the probability mass in both regions should be the same we can write

$$p_X(x) \text{vol}(U) \approx p_Z(z) \text{vol}(f(U)) \quad (39)$$

and therefore

$$p_X(x) = p_Z(f(x)) |R^T f'(x) Q| \frac{\sqrt{|R^T G_Z(f(x)) R|}}{\sqrt{|Q^T G_X(x) Q|}} \quad (40)$$

where the approximation becomes exact by taking the limit of infinitesimally small ϵ . Taking the logarithm, we arrive at the result of Theorem 1. \square

7.2. Loss function

In this section, we consider f_θ parameterized by θ , but drop the subscript for ease of presentation.

Theorem 2. *Let the assumptions of Theorem 1 hold and let $g : \mathcal{M}_Z \rightarrow \mathcal{M}_X$ be the inverse of f . Then, the derivative of the change of variables term has the following trace expression:*

$$\nabla_\theta \log |R^T f'(x) Q| = \text{tr}(R^T (\nabla_\theta f'(x)) g'(f(x)) R). \quad (41)$$

Proof. First, a reminder that $\varphi'(u) = R^T f'(x) Q$ with $\varphi = \psi^{-1} \circ f \circ \phi$. Let $\chi = \varphi^{-1}$, i.e. $\chi = \phi^{-1} \circ g \circ \psi$. Jacobi's formula tells us that

$$\frac{d}{dt} \log |A(t)| = \text{tr} \left(\frac{dA(t)}{dt} A(t)^{-1} \right). \quad (42)$$

Note also that since $\chi(\varphi(u)) = u$, therefore $\chi'(\varphi(u))\varphi'(u) = I$ and $\chi'(\varphi(u)) = \varphi'(u)^{-1}$. Applying Jacobi's formula to $\varphi'(u)$:

$$\nabla_\theta \log |\varphi'(u)| = \text{tr}((\nabla_\theta \varphi'(u))\varphi'(u)^{-1}) \quad (43)$$

$$= \text{tr}((\nabla_\theta \varphi'(u))\chi'(\varphi(u))) \quad (44)$$

and substituting in f and g :

$$\nabla_\theta \log |R^T f'(x) Q| = \text{tr}(\nabla_\theta (R^T f'(x) Q) Q^T g'(f(x)) R). \quad (45)$$

Q does not depend on θ , but R depends on $f(x)$ and hence θ , so it must be considered in the derivative. However,

$$\nabla_\theta \text{tr}(R R^T) = \text{tr}((\nabla_\theta R) R^T + R \nabla_\theta R^T) = 2 \text{tr}(R \nabla_\theta R^T) \quad (46)$$

and since $\text{tr}(R R^T) = \text{tr}(I)$ is a constant, $\text{tr}(R \nabla_\theta R^T) = 0$. Expanding Eq. (45):

$$\begin{aligned} \nabla_\theta \log |R^T f'(x) Q| &= \text{tr}(\nabla_\theta (R^T) f'(x) Q Q^T g'(f(x)) R) \\ &\quad + \text{tr}(R^T \nabla_\theta (f'(x) Q) Q^T g'(f(x)) R). \end{aligned} \quad (47)$$

Since Q is an orthonormal basis for $\mathcal{T}_x \mathcal{M}_X$, $Q Q^T$ is a projection matrix onto $\mathcal{T}_x \mathcal{M}_X$. This is because $(Q Q^T)^2 = Q Q^T Q Q^T = Q Q^T$, using $Q^T Q = I$. As a result, $Q Q^T \text{proj}'(x) = \text{proj}'(x)$. Since g is wrapped inside a projection: $g(z) = \text{proj}_Z(\tilde{g}(z))$, therefore $g'(z) = \text{proj}'_Z(\tilde{g}(z))\tilde{g}'(z)$, so $Q Q^T g'(z) = g'(z)$. Note also that $f'(x)g'(f(x)) = I$ since g is the inverse of f . This simplifies the equation:

$$\begin{aligned} \nabla_\theta \log |R^T f'(x) Q| &= \text{tr}(\nabla_\theta (R^T) R) \\ &\quad + \text{tr}(R^T \nabla_\theta (f'(x)) g'(f(x)) R) \end{aligned} \quad (48)$$

and finally

$$\nabla_\theta \log |R^T f'(x) Q| = \text{tr}(R^T \nabla_\theta (f'(x)) g'(f(x)) R). \quad (49)$$

\square

In the above proof we used the fact that $Q Q^T g'(z) = g'(z)$. Can we use $R R^T f'(x) = f'(x)$ to simplify the equation further? No, we cannot, since the expression involving f' is actually its derivative with respect to parameters, which may not have the same matrix structure as f' . Is it instead possible to use $g'(z) R R^T = g'(z)$ for simplification? If g is implemented as $\text{proj}_Z(\tilde{g}(z))$, this is not necessarily true, as $g'(z)$ might not be a map from the tangent space at z to the tangent space at $g(z)$. For example, if we add a small deviation v to z , where v is orthogonal to the tangent space at z , then $g(z+v)$ might not equal $g(z)$. However, this would mean that derivatives in the off-manifold direction can be non-zero, meaning that $g'(z)v \neq g'(z)R R^T v = 0$

(since RR^T will project v to 0). We can change this by prepending g by a projection:

$$g = \text{proj}_X \circ \tilde{g} \circ \text{proj}_Z. \quad (50)$$

If proj_Z is an orthogonal projection, meaning that proj'_Z is symmetric, the column space and row space of proj_Z will both be the same as those of RR^T , meaning $\text{proj}'_Z(z)RR^T = \text{proj}'_Z$ and hence $g'(z)RR^T = g'(z)$. This leads to the following corollary:

Corollary 3. *Suppose the assumptions of Theorem 1 hold, and g is the inverse of f with the following implementation:*

$$g = \text{proj}_X \circ \tilde{g} \circ \text{proj}_Z \quad (51)$$

where proj_Z is an orthogonal projection. Then the derivative of the change of variables term has the following trace expression:

$$\nabla_\theta \log |R^T f'(x)Q| = \text{tr}((\nabla_\theta f'(x))g'(f(x))). \quad (52)$$

Proof. Take the result of Theorem 2 and use the cyclic property of the trace and the properties of g' discussed above:

$$\begin{aligned} \text{tr}(R^T \nabla_\theta(f'(x))g'(f(x))R) &= \text{tr}(\nabla_\theta(f'(x))g'(f(x))RR^T) \\ &= \text{tr}(\nabla_\theta(f'(x))g'(f(x))). \end{aligned} \quad (53)$$

$$(54)$$

□

We use Hutchinson-style trace estimators to approximate the traces given above. This uses the property that, for a matrix $A \in \mathbb{R}^{n \times n}$ and a distribution $p(v)$ in \mathbb{R}^n with unit second moment (meaning $\mathbb{E}[vv^T] = I$),

$$\mathbb{E}_{p(v)}[v^T Av] = \text{tr}(\mathbb{E}_{p(v)}[v^T Av]) \quad (55)$$

$$= \text{tr}(\mathbb{E}_{p(v)}[vv^T]A) \quad (56)$$

$$= \text{tr}(A) \quad (57)$$

meaning that $v^T Av \approx \text{tr}(A)$ is an unbiased estimate of the trace of A .

We have two variants of the trace estimate derived above, one evaluated in \mathbb{R}^n , the other in \mathbb{R}^m . The first can be estimated using the following equality:

$$\begin{aligned} \text{tr}(R^T \nabla_\theta(f'(x))g'(f(x))R) \\ = \mathbb{E}_{p(u)}[u^T R^T \nabla_\theta(f'(x))g'(f(x))Ru] \end{aligned} \quad (58)$$

$$= \mathbb{E}_{p(v)}[v^T \nabla_\theta(f'(x))g'(f(x))v] \quad (59)$$

$$= \nabla_\theta \mathbb{E}_{p(v)}[v^T \nabla_\theta(f'(x))\text{SG}[g'(f(x))]v] \quad (60)$$

where $p(u)$ has unit second moment in \mathbb{R}^n and $p(v)$ is the distribution of Ru , which lies in the tangent space at x

and has unit second moment in that space by which we mean $\mathbb{E}[vv^T] = RR^T$. An example of such a distribution is the standard normal projected to the tangent space, i.e. $v = RR^T \tilde{v}$ where \tilde{v} is standard normal.

In the second case, we can just sample from a distribution with unit second moment in the embedding space \mathbb{R}^m :

$$\begin{aligned} \text{tr}(\nabla_\theta(f'(x))g'(f(x))) \\ = \nabla_\theta \mathbb{E}_{p(v)}[v^T \nabla_\theta(f'(x))\text{SG}[g'(f(x))]v]. \end{aligned} \quad (61)$$

7.3. Variance reduction

When using a Hutchinson trace estimator with standard normal $v \in \mathbb{R}^n$, we can reduce the variance of the estimate by scaling v to have length \sqrt{n} (see [18]). The scaled variable will still have zero mean and unit covariance so the estimate remains unbiased, but the variance is reduced, with the effect especially pronounced in low dimensions.

While we can take advantage of this effect in both our options for trace estimator, the effect is more pronounced in lower dimensions, so we reduce the variance more by estimating the trace in an n -dimensional space rather than an m -dimensional space. Hence the first version of the trace estimator, where v is sampled from a distribution in $\mathcal{T}_x \mathcal{M}_X$ is preferable in this regard.

Let's provide some intuition with an example. Suppose $n = 1$, $m = 2$ and $R = (1, 0)^T$. We want to estimate the trace of $A = \text{diag}(1, 0)$. Using the first estimator, we first sample $v = RR^T \tilde{v}$ with \tilde{v} standard normal which results in $v = (u, 0)^T$ where $u \in \mathbb{R}$ is standard normal. Then we scale v so it has length $\sqrt{n} = 1$. This results in $v = (r, 0)^T$ where r is a Rademacher variable (taking the value -1 and 1 with equal probability). The trace estimate is therefore $r^2 = 1$, meaning we always get the correct answer, so the variance is zero. The second estimator samples v directly from a 2d standard normal, then scales it to have length $\sqrt{m} = \sqrt{2}$. Hence v is sampled uniformly from the circle with radius $\sqrt{2}$. We can write $v = \sqrt{2}(\cos \theta, \sin \theta)^T$ with θ sampled uniformly in $[0, 2\pi]$. The estimate $v^T Av = 2 \cos^2 \theta$. This is a random variable whose mean is indeed 1 as required but has a nonzero variance, showing that the variance is higher when estimating in the m -dimensional space.

For this reason, we choose the first estimator, sampling v in the tangent space at x . This also simplifies the definition of g , meaning that we don't have to prepend it with a projection.

8. Experimental details

In accordance with the details provided in Sec. 4.3, our approach incorporates multiple regularization loss components in addition to the negative log-likelihood objective.

Hyperparameter	Value
Layer type	ResNet
Residual blocks	2
Inner depth	5
Inner width	512
Activation	ReLU
β_{R}^x	500
β_{R}^z	0
β_{U}	10
β_{P}	10
Latent distribution	uniform
Optimizer	Adam
Learning rate	5×10^{-3}
Scheduler	Exponential w/ $\gamma = 1 - 10^{-5}$
Gradient clipping	1.0
Weight decay	3×10^{-5}
Batch size	1,024
Step count	585,600

Table 6. Hyperparameter choices for the rotation experiments. β_{U} and β_{P} are the same for both the sample and latent space.

Dataset	Number of instances	Noise strength
Volcano	827	0.008
Earthquake	6120	0.0015
Flood	4875	0.0015
Fire	12809	0.0015

Table 7. Dataset overview for the earth data experiments. Each dataset is split into 80% for training, 10% for validation and 10% for testing.

This results in the final loss expression:

$$\mathcal{L} = \mathcal{L}_{\text{NLL}} + \beta_{\text{R}}^{x/z} \mathcal{L}_{\text{R}}^{x/z} + \beta_{\text{U}}^{x/z} \mathcal{L}_{\text{U}}^{x/z} + \beta_{\text{P}}^{x/z} \mathcal{L}_{\text{P}}^{x/z}. \quad (62)$$

For each of the terms, there is a variant in x - and in z -space, as indicated by the superscript. In detail:

The first loss \mathcal{L}_{R} represents the reconstruction loss:

$$\mathcal{L}_{\text{R}}^x = \mathbb{E}_{x \sim p_{\text{data}}} [d(x, g_{\phi}(f_{\theta}(x))),] \quad (63)$$

$$\mathcal{L}_{\text{R}}^z = \mathbb{E}_{x \sim p_{\text{data}}} [d(f_{\theta}(x), f_{\theta}(g_{\phi}(f_{\theta}(x))))]. \quad (64)$$

Here $d(x, y) = \|x - y\|^2$ is the standard reconstruction loss in the embedding space. This could be replaced with a distance on the manifold. However, this would be more expensive to compute and since we initialize networks close to identity, the distance in the embedding space is almost equal to shortest path length on the manifold.

In order to have accurate reconstructions outside of training data, we also add reconstruction losses for data uniformly sampled on the manifold, both for x and z :

$$\mathcal{L}_{\text{U}}^x = \mathbb{E}_{x \sim \mathcal{U}(\mathcal{M})} [d(x, g_{\phi}(f_{\theta}(x))),] \quad (65)$$

$$\mathcal{L}_{\text{U}}^z = \mathbb{E}_{x \sim \mathcal{U}(\mathcal{M})} [d(z, f_{\theta}(g_{\phi}(z)))] \quad (66)$$

Hyperparameter	Value
Layer type	ResNet
residual blocks	4
Inner depth	2
Inner width	256
Activation	sin
β_{R}^x	10^5
β_{R}^z	0
β_{U}	2×10^2
β_{P}	0
Latent distribution	VMF-Mixture ($n_{\text{comp}} = 5$)
Optimizer	Adam
Learning rate	2×10^{-4}
Scheduler	onecyclelr
Gradient clipping	10.0
Weight decay	5×10^{-5}
Batch size	32
Step count	$\sim 1.2\text{M}$

Table 8. Hyperparameter choices for the earth data experiments. β_{U} and β_{P} are the same for both the sample and latent space.

Dataset	Number of instances	Noise strength
General	138208	0
Glycine	13283	0
Proline	7634	0
Pre-Proline	6910	0
RNA	9478	1×10^{-2}

Table 9. Details on the torus datasets. Each dataset is randomly split into a train dataset (80%), validation dataset (10%) and test dataset (10%). During training, we add Gaussian noise with mean zero and standard deviation given by ‘noise strength’ to the data, to counteract overfitting.

Finally, we make sure that the function learned by the neural networks is easy to project by regularizing the distance between the raw outputs by the neural networks in the embedding space and the subsequent projection to the manifold (compare Eq. (9)):

$$\mathcal{L}_{\text{P}}^x = \mathbb{E}_{x \sim p_{\text{data}}} [\|g_{\phi}(f_{\theta}(x)) - \tilde{g}_{\phi}(f_{\theta}(x))\|^2], \quad (67)$$

$$\mathcal{L}_{\text{P}}^z = \mathbb{E}_{x \sim p_{\text{data}}} [\|f_{\theta}(x) - \tilde{f}_{\theta}(x)\|^2]. \quad (68)$$

If these superscripts are not specified explicitly in the following summary of experimental details, we mean $\beta^x = \beta^z$.

8.1. Special orthogonal group

The special orthogonal group data set is synthetically generated. We refer to [10] for a description of the data generation process. They use an infinite stream of samples. To emulate this, we generate a data set of 10^7 samples from their code, of which we reserve 1,000 for validation during

Hyperparameter	Value (\mathbb{T}^2)	Value (\mathbb{T}^7)
Layer type	ResNet	ResNet
residual blocks	6	2
Inner depth	2	2
Inner width	256	256
Activation	SiLU	SiLU
$\beta_{\mathbf{R}}^x$	100	1000
$\beta_{\mathbf{R}}^z$	100	100
$\beta_{\mathbf{U}}^x$	100	100
$\beta_{\mathbf{U}}^z$	0	1000
$\beta_{\mathbf{P}}$	0	0
Latent distribution	uniform	uniform
Optimizer	Adam	Adam
Learning rate	1×10^{-3}	1×10^{-3}
Scheduler	onecyclelr	onecyclelr
Gradient clipping	-	-
Weight decay	1×10^{-3}	1×10^{-3}
Batch size	512	512
Step count	$\sim 60\text{k}$	$\sim 120\text{k}$

Table 10. Details on the model architecture, loss weights and optimizer parameters for the torus datasets. We use the same configuration for all protein datasets on \mathbb{T}^2 .

training and 5,000 for testing. We vectorize the 3×3 matrices before passing them into the fully-connected networks. All training details are given in Tab. 6.

8.2. Earth data

We follow previous works and use a dataset split of 80% for training, 10% for validation and 10% for testing. For the earth datasets we use a mixture of 5 learnable Von-Mises-Fisher distributions for the target latent distribution. We base our implementation on the `hyperspherical_vae` library [9]. In order to stabilize training we apply a small amount of Gaussian noise to every batch (see table 7) and project the resulting data point back onto the sphere. Other training hyperparameters can be found in table 8.

8.3. Tori

The torus datasets are randomly split into a train dataset (80%), validation dataset (10%) and test dataset (10%). To counteract overfitting, we augment the RNA dataset with random Gaussian noise. The noise strength and total number of instances is reported in Tab. 9. We use a uniform latent distribution. While we train for $\sim 60\text{k}$ steps on the protein datasets (General, Glycine, Proline and Pre-Proline), we train for $\sim 120\text{k}$ steps on the RNA datasets, both with a batch size of 512. Further hyperparameters used in training can be found in Tab. 10.

8.4. Libraries

We base our code on `PyTorch` [40], `PyTorch Lightning` [13], `Lightning Trainable` [25], `Numpy` [19], `Matplotlib` [21] for plotting and `Pandas` [31, 47] for data evaluation. We use the `geomstats` [32, 33] package for embeddings and projections.